Numerical study on thermal contact resistance of 8-harness satin woven pierced composite

Xing-Jie Ren [a], Yan-Jun Dai [a], Jian-Jun Gou [b], Wen-Quan Tao [a],[*]

[a] *Key Laboratory of Thermo-Fluid Science and Engineering of MOE, School of Energy and Power Engineering, Xi'an Jiaotong University, Xi'an, Shaanxi, 710049, China*
[b] *Shaanxi Aerospace Flight Vehicle Key Laboratory, School of Astronautics, Northwestern Polytechnical University, Xi'an, 710072, China*

ARTICLE INFO

ABSTRACT

In this paper, thermal contact resistance between a pair of 8-harness satin woven pierced composites is numerically investigated when the interface gaps are filled with air. Numerical model of the rough surfaces is based on measured results of actual specimens by a microscope. The results show that thermal contact resistance decreases with an increase in both loading pressure and temperature. The effects of interfacial thermal radiation on the predicted thermal contact resistance increase with an increase in temperature, but less than 5%. The percentage of heat transfer rate through solid contact regions occupies less than 17% of overall heat transfer rate for the cases studied with solid thermal conductivity around 10 $W \cdot m^{-1} \cdot K^{-1}$ and loading pressure up to 2.37 MPa. For the studied composite pair (averaged surface roughness of 12.30 μm, 10.54 μm) thermal contact resistance is in a range of 9.8×10^{-4} - 5.7×10^{-4} $K \cdot m^2 \cdot W^{-1}$.

1. Introduction

All surfaces of engineering materials are rough under a certain magnification even they are apparently smooth. Hence, for two contacting solid surfaces, because there are random hills and valleys in the surfaces, actual contact only exists at some discrete spots and non-contact regions form gaps filled with air or other medium. Generally, thermal conductivity of solid is exceedingly higher than that of air or other medium, so when heat flow goes through the contact interfaces, the heat flow will shrink towards the actual contact spots and the heat flux will be distributed nonuniformly, as shown in Fig. 1 [1]. Consequently, a temperature difference will occur at the contact interfaces, and such a phenomenon is named as thermal contact resistance (TCR). Its value equals to the quotient of temperature difference between two contact interfaces and the average heat flux through the interfaces, as shown by Eq. (1):

$$R = \frac{\Delta T}{q} \qquad (1)$$

where R ($K \cdot m^2 \cdot W^{-1}$) is thermal contact resistance, and ΔT (K), q(W/m^2) are the temperature difference and heat flux through the contact interface, respectively.

Thermal contact resistance dramatically influences the efficiency and even safety of the engineering apparatuses, so it should be seriously taken into consideration in many engineering designs and applications, such as heat-assisted magnetic recording (HAMR) [2], electronic packaging [3], finned tube exchangers [4,5], fuel cells [6,7], spacecraft thermal controls [8,9], etc. For instance, one of the main reasons that makes smartphones run slowly and causes thermal discomfort for users is their low efficiency of heat dissipation of CPUs to the supporting substrate [10], and decreasing thermal contact resistance between CPUs and the supporting substrate is one of the meaningful methods for efficient heat dissipation of smartphones.

Although it was studied before 1940s, thermal contact resistance still deserves much detailed research. Previous studies have revealed that loading pressure [11], temperature, surface topography (roughness, flatness, waviness) [12], coatings of materials [13,14], and material properties can all influence thermal contact resistance, but the specific influence characteristics of each factor depend on practical circumstances and materials. Among different influencing factors, the material surface topography and material type are two very important factors, hence received much attention of researchers. Taking some papers published in recent five years as examples. Zhang and Cui [15] conducted a study of effect of surface roughness on thermal contact resistance of five types of aluminium alloy materials with the surface R_a ranging from 0.2 μm to 4.2 μm. Dou et al. [16] experimentally studied the effect of contact pressure, interface temperature and surface

---

Nomenclature

A_C	Actual contact area	R_a	Arithmetical mean roughness
A_N	Nominal contact area	S	Deflection stress tensor
c	Specific heat capacity	T	Temperature
d	Clearance distance	T_{ave}	Interface average temperature
D^e	Elasticity matrix	U_i	Displacement in i direction
D^p	Plasticity matrix	UR_i	Potation displacement in three spatial angles
E	Elasticity modulus	x, y, z	Cartesian coordinates
E_p	Plasticity modulus	γ	Shear strain
E_t	Slop of the stress-strain curve	δ	Relative deviation
F_N	Squeezing force	ε	Total mechanical strain
F	Effective view factor	ε^e	Elastic strain
f_i	Component of the unit body force in i direction	ε^p	Plastic strain
G	Shear modulus	ν	Poisson's ratio
k	Gap conductance	ρ	Density of the composite material
P	Pressure	σ	Normal stress
q	Heat flux, specific	σ_{SB}	Stefan-Boltzmann constant
q_{ra}	Heat flux contributed by thermal radiation	σ_s	Elastoplasticity stress
R	Thermal contact resistance	λ	Thermal conductivity
		τ	Shear stress
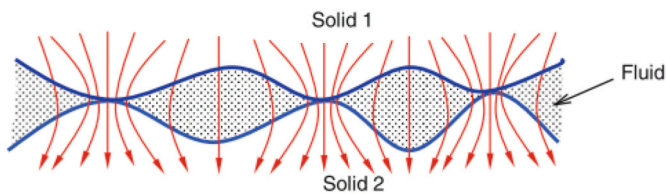
Fig. 1. Heat flow through a contact interface [1].

roughness on thermal contact resistance for four pairs of stainless steel surfaces with R_a of 0.25 μm, 0.4 μm, 1.18 μm, 2.0 μm. Joseph et al. [17] studied the effects of both thermal and pressure load on thermal contact resistance across dissimilar joints at cryogenic temperature. In their research, the joints are formed by titanium alloy, stainless steel and aluminium alloy. The surface roughness was controlled between 1 and 2 μm. Zhang et al. [18] conducted a study about the effect of heat flux direction on thermal contact resistance of samples of 99.999% standard pure copper pairs with surface roughness 1 μm and Elkonite copper–tungsten alloy 30W3 pairs with surface roughness 0.5 μm. It can be seen that all the studies mentioned above were based on specific materials and surface condition, and the TCR data obtained can only be applied to their test conditions. It is the authors' understanding that the study on TCR at present is something like the study on experimental convective heat transfer years ago: even though the test method and the way of data reduction are all the same, still a large number of paper were published for different specific convective situations. Thus, for the experimental study on thermal contact resistance, for different materials and their surface conditions specific studies are needed to get their TCR data.

Besides analytical model [19–21] and experiments study [22–24] on thermal contact resistance, rapidly increasing computational capacity makes researchers convenient to conduct numerical research on thermal contact resistance. For example, Zhang et al. [25] developed a random model of surface roughness to study the effects of contact pressure, thermal conductivity of the interstitial medium, and the mean absolute slope of the rough surface on thermal contact resistance. In their study, a grid system with equi-peripheral intervals in the azimuthal direction was developed to express reasonably the real contact spot distribution, and a network method based on this grid system was used to calculate the TCR. They also mentioned that one of the main factors to accurately

predict thermal contact resistance is to characterize the actual surface topography quantitatively and accurately. This opinion is widely agreed by researchers and the authors of [26–28] reconstructed the rough contact surfaces based on the actual surface topography measured by a high-resolution microscope. Gou et al. [26] developed a numerical model to simulate thermal contact resistance for material pairs of Ti–6Al–4V–Ti6Al–4V and C/C–SiC—high temperature ceramic (HTC). Though the numerical model was validated by experiments, the shape and size of the numerical model were different from the actual specimen size. In addition, a constant gap conductance was assumed in Ref. [26] to handle the heat transfer at the interface through air gaps, which is seemingly a rough assumption. Dai et al. [27] measured the surface topography by a 3D optical microscope and adopted the software Abaqus to numerically predict TCR of Ti–6Al–4V–Ti6Al–4V. The shape and size of the numerical model coincided with the actual specimens, and the gap conductance was determined according to the clearance distance between two contact interfaces. Their test-validated results showed that the developed prediction method had a satisfying precision and accuracy with all the deviations between numerical and experimental TCR results being within 10%. Most of the TCR studies mentioned above are all for homogeneous and isotropic materials.

In many engineering fields, non-isotropic composite materials are widely used. For its high strength, low density and thermal conductivity [29], C/C–SiC composites can be used in the multi-layer thermal protection systems of hypersonic vehicles [30–32], and TCR data are very important input information for the design of such systems. Marchetti et al. [33] studied the thermal contact resistance of composite materials such as glass and carbon fiber-epoxy for space applications with pressure ranged from 0 to 28 MPa and temperature from 30 to 90 °C. Liu et al. [34] experimentally studied the effects of temperature and pressure on the thermal contact resistance of the interface formed by C/C composite and Inconel alloy. Ren et al. [28] conducted numerical study on thermal contact resistance of 3D C/C–SiC needled composites. The studied composite in Ref. [28] is an orthotropic material. The terminology orthotropic thermal conductivity means that the thermal conductivities of the main diagonal direction in a thermal conductivity tensor are not zero, and other elements are zero [29].

From above brief presentation it is clear that not only material type, but also the structure of composite has strong effect on TCR. Taking the orthotropic material composite as an example. There are usually two different woven structures, satin woven and needled woven, and the schematic pictures of the two composites are shown in Fig. 2. The

components of the materials are both C/C–SiC. Because very different woven structures their behavior in thermal conductivity and TCR are quite different. The woven structure studied in Ref. [28] is the needled one. In this paper the satin woven structure will be studied.

In this paper, numerical simulation for thermal contact resistance between a pair of 8-harness satin woven composite is conducted, and the numerical model is validated by experiments. This composite uses carbon fibers as reinforcing fibers and its matrix is C and SiC. As mentioned above, the surface topography model in this paper is based on the actual measurement of a pair of specimens of 8-harness satin woven composite. The commercial software Abaqus is used to solve the governing equations, and the effects of temperature, pressure and interfacial thermal radiation on thermal contact resistance are investigated.

The following parts of this paper are arranged as follows. Section 2 is a brief introduction of the modeling process. Section 3 introduces the governing equations, computational cases, the boundary conditions and material properties. Section 4 gives the numerical results and Section 5 draws the conclusions.

2. Physical and numerical model

2.1. Reconstruction of rough contact interfaces

The actual topography of the contact interfaces greatly influences thermal contact resistance. Thereby, in the simulation of thermal contact resistance, a crucial procedure is the reconstruction of rough contact interfaces. In this paper, the rough contact interfaces are reconstructed based on the measured actual topographies of the composite specimens. The process from surface topography measurement to the input data of numerical simulation includes measuring and importing two steps. First, measuring the surface topography of the specimens by a microscope named Bruker Contour GT-K. Second, importing the measured surface topography data into a pre-processing software ANSA to construct the numerical model for Abaqus conveniently. The measured arithmetical mean roughness, denoted by R_a, of the two specimens for testing TCR are 12.30 μm and 10.54 μm, respectively. Fig. 3(a) and Fig. 3(b) demonstrate the actual surface and measured graphical result of the one specimen, respectively. Fig. 3 (c) and Fig. 3(d) show the measured asperity distributions along two diameters perpendicular to each other, denoted by x and y in Fig. 3 (b). As we can see that the asperity distributions are totally random. One well major representation of such randomly distribution is its arithmetical mean roughness R_a, and it is also well accepted in the study of thermal contact resistance for

representing surface roughness characteristics [15–18]. In this paper we adopt this practice to represent surface roughness property. It is our believe that if two pairs of surfaces of the same material have their average surface roughness the same, the TCR of the two pairs of surfaces should be the same with an acceptable range of deviation. Fig. 4 depicts the reconstructed rough surface used in Abaqus.

2.2. Computational domain and mesh generation

The domain can be divided into the top part and the bottom part, as seen in Fig. 5 (a). Each part is 10 mm in height and 24 mm in radius. For the two contact interfaces, the lower contact interface is interface I, and the upper contact interface is interface II. After the rough surfaces are reconstructed, the mesh can be generated based on the reconstructed rough surfaces. The hexahedral meshes are applied to the whole numerical model, and the meshes near the contact interfaces are refined to ensure the precision of the results, as seen in Fig. 5 (b). The total number of nodes and meshes are 1859418 and 1778944 respectively, determined by the grid-independence examination.

3. Governing equations and boundary conditions

TCR prediction includes both mechanical and thermal processes, hence both governing equations of mechanics (displacement and deformation) and heat conduction are needed. However, once the displacement and deformation of each element are determined, the major work is the computation of heat conduction through the contacted pair of elements. Thus, for the simplicity of presentation, only the governing equation of thermal process is presented below, the governing equations of the mechanical process can be found in Appendix A.

3.1. Heat conduction equation

In this paper, we only focus on thermal contact resistance at a steady state of heat conduction, and no inner heat source is imposed in the numerical model. As indicated in the Introduction, 8-harness satin woven pierced composite is a thermal orthotropic material, thus, the governing equation of steady-state heat conduction can be expressed by Eq. (2):

$$\frac{\partial}{\partial x}\left(\lambda_{xx}\frac{\partial t}{\partial x}\right) + \frac{\partial}{\partial y}\left(\lambda_{yy}\frac{\partial t}{\partial y}\right) + \frac{\partial}{\partial z}\left(\lambda_{zz}\frac{\partial t}{\partial z}\right) = 0 \tag{2}$$

where, λ_{xx}, λ_{yy}, λ_{zz} are the thermal conductivities of the main diagonal

(a) Satin woven pierced composite

(b) Needled woven composite
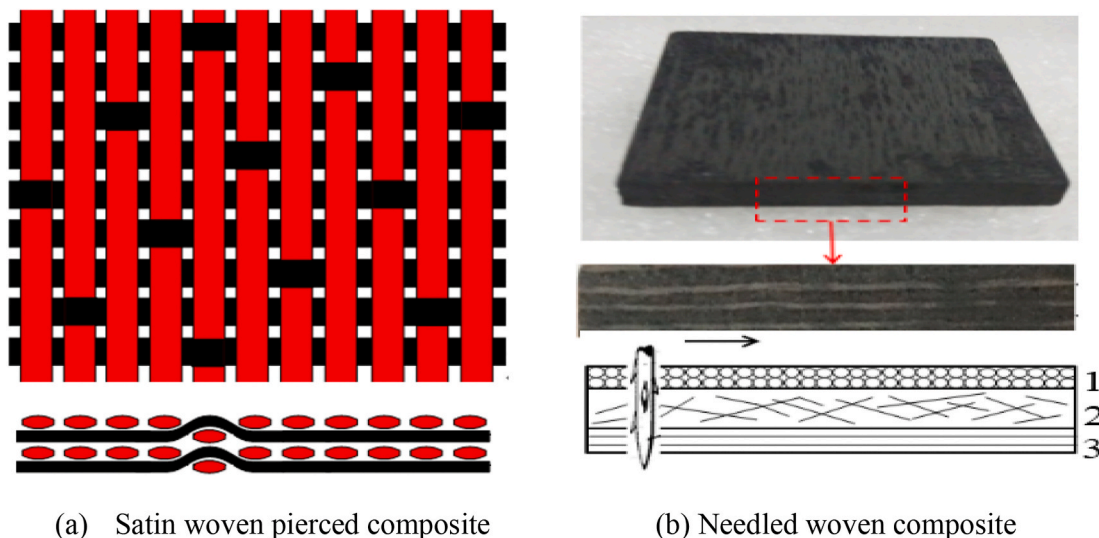
Fig. 2. Two woven structures of composite materials [35].

(a)   Actual material surface

(b)   Measured graphical result

(c)   Measured asperity distribution in *x* direction

(d)   Measured asperity distribution in *y* direction
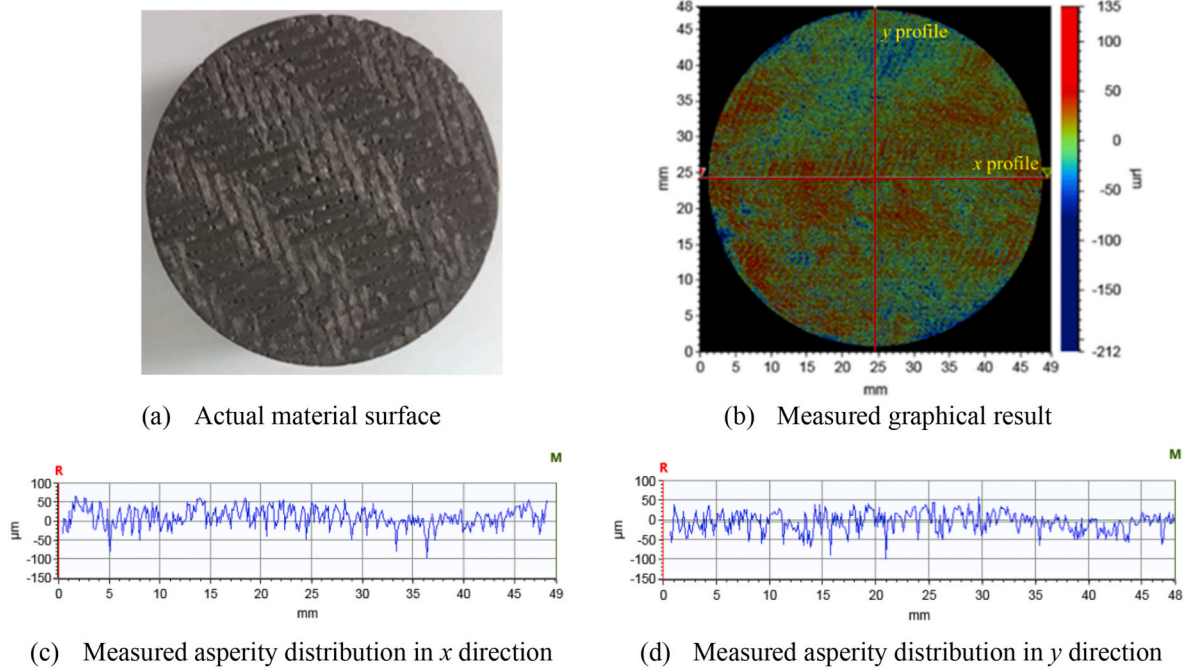
Fig. 3. Material surface.
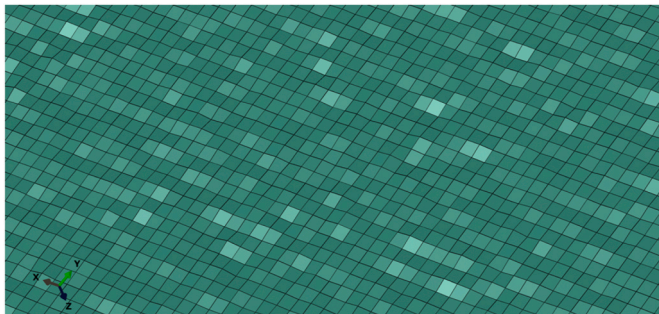
Fig. 4. Reconstructed rough surface.

direction in a thermal conductivity tensor.

3.2. Gap conductance

To predict thermal contact resistance, a key parameter is the gap conductance between two contact interfaces. In Abaqus, the heat conduction between the contact interfaces is expressed by Eq. (3):

$$q = k(T_A - T_B) \tag{3}$$

where q is the heat flux crossing the interface from point A on one surface to point B on the other. T_A and T_B are the temperatures of the two points on the surfaces, termed slave surface and master surface respectively, and k is the gap conductance. Point A is a node on the slave surface; and point B is the location on the master surface contacting the slave node or, if the surfaces are not in contact, the location on the master surface with a surface normal that intersects the slave node. As for the parameter k, it can be defined as a function of clearance distance, as shown in Eq. (4):

(a) Meshed numerical model

(b) Meshes near the contact interface
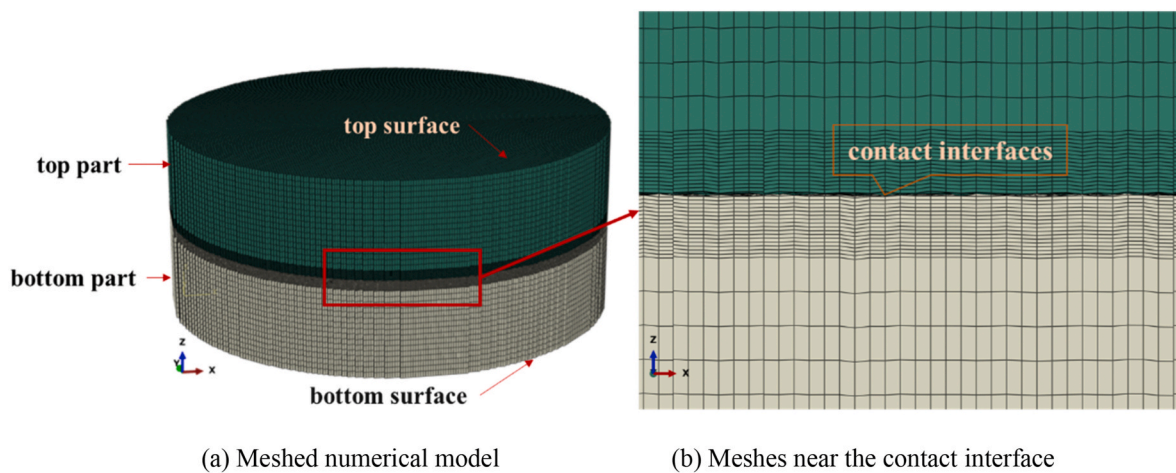
Fig. 5. Meshed model.

$$k = k(d, \overline{T}) = \frac{\lambda(\overline{T})}{d} \tag{4}$$

where, d is the clearance distance between point A and point B, which can be obtained from the generated upper and lower surface meshes; $\overline{T} = \frac{T_A + T_B}{2}$ is the average temperature of the surfaces at point A and point B and used as the reference temperature of the medium in the gap. In this study, the medium at the interface is air, then $\lambda(\overline{T})$ is the thermal conductivity of air at temperature $\overline{T}$.

3.3. Thermal radiation at the contact interface

Thermal radiation at contact interfaces is considered in this paper. Abaqus defines the thermal radiation between corresponding points as Eq. (5):

$$q_{ra} = C(T_A^4 - T_B^4) \tag{5}$$

where q_{ra} is the heat flux crossing the gap at this point from surface A to surface B, and T_A and T_B are the temperatures in K of the two surfaces, respectively, and the coefficient C is given by

$$C = \frac{F\sigma_{SB}}{\frac{1}{\varepsilon_A} + \frac{1}{\varepsilon_B} - 1} \tag{6}$$

where σ_{SB} is the Stefan-Boltzmann constant, and ε_A, ε_B are the surface emissivities. And F is the effective view factor. In this paper, we assume the emissivity of the material as 0.9, and the effective view factor is set as 1.0, since the top and bottom surfaces are very close to each other. However, it should be noted that the distance is not so small as can be compared with λ_{th} determined by Wien's displacement law for which the near-field radiation plays role [36], so we use Stefan-Boltzmann law to calculate thermal radiation between the interfaces.

It should be mentioned that T_A and T_B in Eqs. (3 and 5) are not boundary conditions, and they can be obtained by solving the algebraic equations determined by the FEM method. Actually, we define the contact interaction between two contact interfaces, thus, Abaqus can recognize the interaction interface and handle the interaction information; then Eq. (3) and Eq. (5) are applied to calculate the needed information between two interaction interfaces.

It should also be mentioned that only the thermal radiation of the air gaps at the contact interface is considered, and the thermal radiation between the specimens and environment is neglected because the lateral surfaces are supposed to be well-insulated and where the adiabatic boundary condition is applied.

3.4. Boundary conditions

The boundary conditions adopted in the present study are described as follows.

3.4.1. Mechanical boundary conditions

We can obtain the contact state and distribution between two solid interfaces through the mechanical analysis. The mechanical boundary conditions and mechanical parameters are shown in Table 1. Where, U_1, U_2, U_3 represent the displacements in x, y, z directions, respectively, and UR_i ($i = 1, 2, 3$) represents the rotation displacements in three spatial angles. P_i is the loading pressure perpendicularly applied to the contact

interfaces. "\" indicates that no restriction is imposed for that boundary. Two key parameters, the elastic modulus and Poisson's ratio are 60 GPa and 0.12, respectively.

Two points should be noted here. First, Interface I is the face-up interface of the bottom test specimen, and Interface II is the face-down interface of the top one. Second, these two interfaces are actually within the solution domain, hence no any boundary conditions should be imposed.

3.4.2. Thermal boundary conditions

The thermal boundary conditions are listed in Table 2. In the table, T_{up} and T_{down} are the temperatures applied to top surface and bottom surface depicted in Fig. 5 (a). Our simulation is in a wide range of temperature; thus, temperature-dependent thermal conductivity of the material must be given to accomplish the simulation. Table 3 lists the temperature-dependent thermal conductivity of 8-harness satin woven composite. The thermal conductivity is measured by laser flash method. For the temperatures not indicated in Table 3, the corresponding thermal conductivities are interpolated from the table. Convection heat transfer in gaps is neglected because the gaps between the contact interfaces are too narrow to cause convection [1].

3.5. Computational cases

To study the effect of pressure and temperature on thermal contact resistance, three loading pressures (1.03 MPa, 1.54 MPa and 2.37 MPa) are selected to conduct the simulation under different temperatures. The details of the computational cases can be seen in Table 4, where the number in the parenthesis is the temperature difference between T_{down} and T_{top}. These temperature data come from experimental measurements, thus we can validate our numerical model with experimental results. The major differences between the seven cases are the level of temperature and temperature difference between T_{down} and T_{top}, ranging from about 50 °C of Case A to about 154 °C of Case F.

4. Results and discussions

4.1. Actual contact area

Actual contact area is one of the central characteristics of the contact between rough surfaces [37]. Fig. 6 shows the predicted dependency relationship between the loading pressure and the percentage of the actual contact area. We can see that the ratio, A_C/A_N, experiences an approximately linear increase with an increase in loading pressure. Previous studies [25,38,39] also provided similar results. The linear variation between actual contact area and load is corresponding to mainly elastic deformation. If plastic deformation occurs, the variation trend will be changed depending on the load, mechanical properties of the materials and the actual topography of the contact interfaces. Revealing the contact deformation mechanism in detail is a great challenge to researchers, and [37,40–44] can be consulted and further study is still needed.

4.2. The deformation at the contact interface

Fig. 7 (a) shows the Mises stress distribution in interface I at 1.03 MPa. It can be seen that the stress distribution is extreme non-uniform

Table 1
Mechanical boundary conditions.

location	U_1	U_2	U_3	UR_i ($i = 1,2,3$)	P (MPa)
top surface	0	0	\	\	P_i
top lateral wall	0	0	\	0	\
bottom lateral wall	0	0	\	0	\
bottom surface	0	0	0	0	\

Table 2
Thermal boundary conditions.

location	T	Q
top surface	T_{up}	\
bottom surface	T_{down}	\
bottom lateral wall	\	0, adiabatic
top lateral wall	\	0, adiabatic

Table 3

Temperature-dependent thermal conductivity of 8-harness satin woven composite.

$T/°C$	$\lambda_{xx}/W·m^{-1}·K^{-1}$	$\lambda_{yy}/W·m^{-1}·K^{-1}$	$\lambda_{zz}/W·m^{-1}·K^{-1}$
25	9.15	9.15	5.19
100	11.25	11.25	6.53
200	12.70	12.70	7.41
300	13.08	13.08	7.71
400	13.33	13.33	7.92
500	13.43	13.43	8.02

Table 4

Computational cases.

$Pi/$ MPa	1.03		1.54		2.37	
$T/°C$	T_{up}	T_{down}	T_{up}	T_{down}	T_{up}	T_{down}
Case A	165.0	2218.2 (53.2)	158.5	208.2 (49.7)	154.9	204.5 (49.6)
Case B	221.7	295.4 (72.8)	208.6	278.5 (69.9)	203.1	273.2 (70.1)
Case C	276.9	372.8 (95.9)	254.5	344.1 (89.6)	249.0	339.4 (90.4)
Case D	330.1	446.1 (116)	304.6	413.9 (109.3)	294.5	403.4 (108.9)
Case E	401.1	5445.9 (144.8)	353.1	483.1 (130.0)	330.0	453.8 (123.8)
Case F	420.5	574.0 (153.5)	417.5	570.3 (152.8)	366.1	505.8 (139.7)

Equation	y = a + b*x
Plot	B
Weight	No Weighting
Intercept	7.67512E-4 ± 2.00688E
Slope	0.00477 ± 4.80987E-5
Residual Sum of Squar	1.15579E-6
Pearson's r	0.99959
R-Square (COD)	0.99919
Adj. R-Square	0.99908
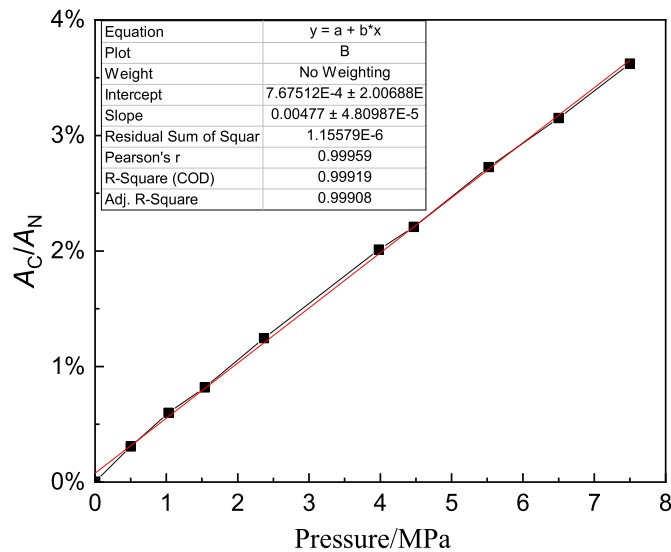
Fig. 6. Dependency of A_C/A_N with an increasing loading pressure.

because of the roughness. When two solid surfaces are brought into contact, the deformation at the contact interface may has three types: elastic deformation, elastic-plastic deformation and plastic deformation. Ten contact nodes and 10 noncontact nodes at the interface are selected to show the z coordinate variations. Fig. 7 (b) shows the z coordinate variation of 10 noncontact nodes at different loading pressures. As we can see, the node coordinate variations increase with an increase in loading pressure, and different nodes have the same variation trend. The z coordinate variations of the contact nodes are much larger (Fig. 7 (c)). Besides, different node has different variation amplitudes. Combined with Fig. 6, it may be concluded that the deformation of most contact points is elastic. Further study is needed on how to identify deformation characteristics of each point.
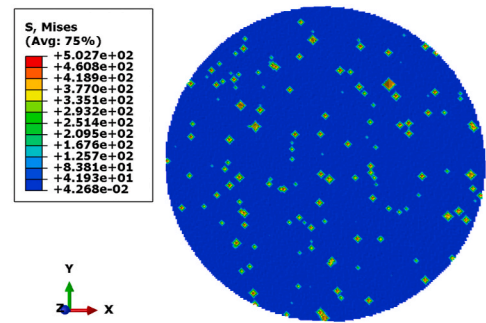
(a) Mises stress distribution of interface I at 1.03MPa
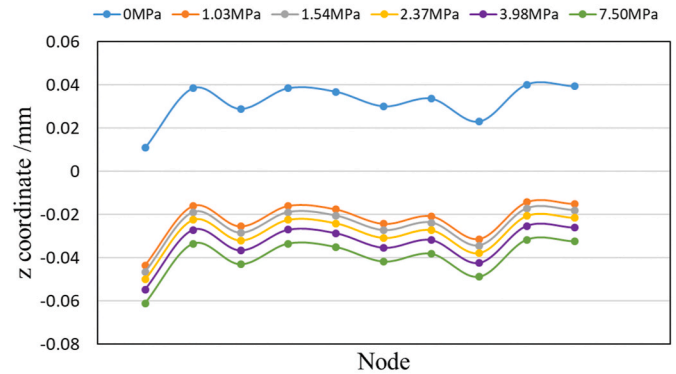
(b) z coordinate variation of 10 noncontact nodes at different loading pressures
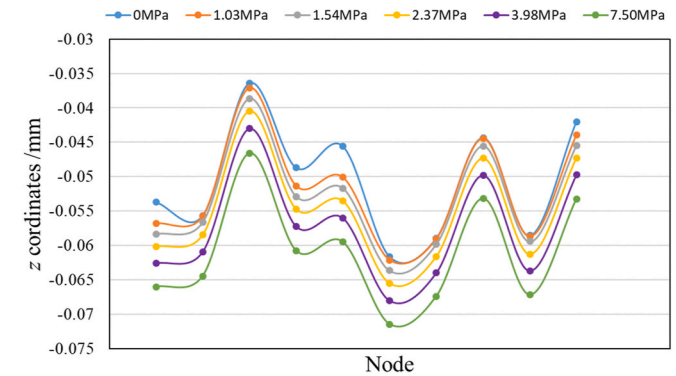
(c) z coordinate variation of 10 contact nodes at different loading pressures

Fig. 7. The deformation at the contact interface.

4.3. Local and average interface temperature and heat flux

Taking the results at $P = 1.54$ MPa as an example, the predicted heat flux and temperature distributions at the interface are presented in Fig. 8.

In Fig. 8 HFL in legend represents the heat flux, and its unit is " $\times 10^2$ W/m^2 "75%" in the legend is the default averaging threshold in Abaqus. The default averaging threshold is a sentence threshold whether several computational values at a same node is to be averaged. It can be roughly observed that where there is a high heat flux there the two interface temperatures are higher.

The average interface temperature and heat flux for the seven cases studied without considering radiation are presented in Fig. 9. As indicated in Table 4, from Case A to Case F both interface temperature level and temperature difference level increase, hence both the predicted interface averaged temperature and heat flux increase with the case order. For the same case the difference in heat flux is mainly dependent on the specified temperature at the top and bottom surfaces.

(a) Heat flux

Interface I

Interface II
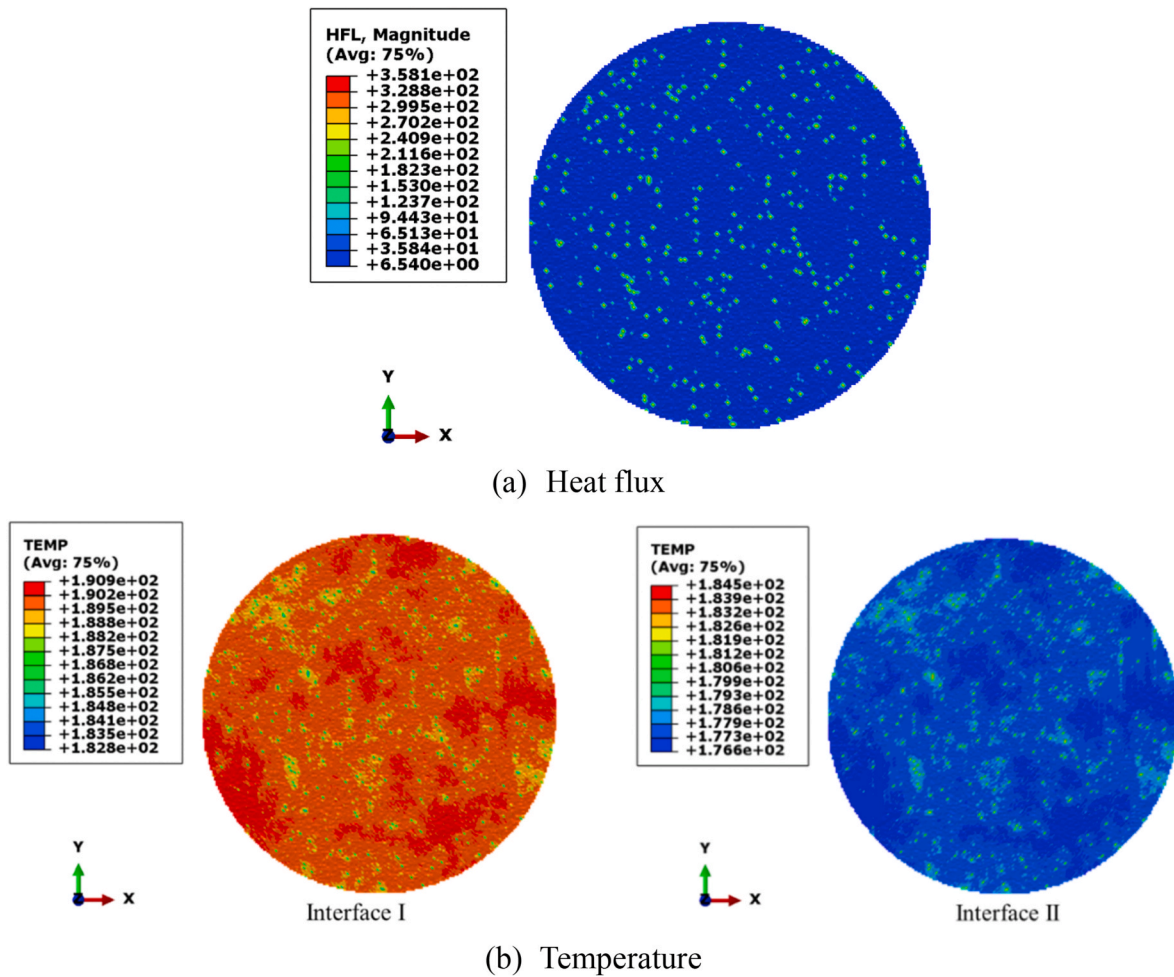
(b) Temperature

Fig. 8. Interface heat flux and temperature ditributiond at $P = 1.54$ MPa.

(a) Temperature
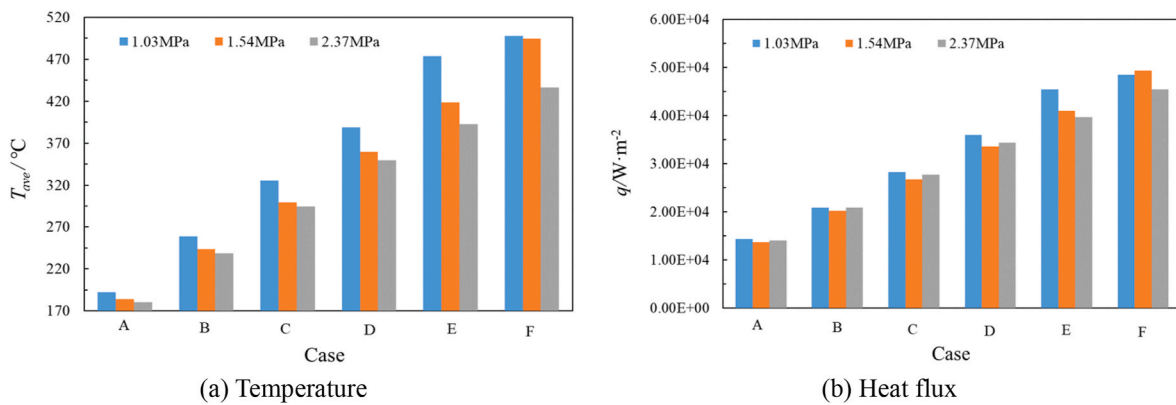
(b) Heat flux

Fig. 9. Average interface temperature and heat flux.

4.4. Effect of thermal radiation

Because two interfaces only contact at some discrete spots, the effect of thermal radiation between the gaps of contact interfaces is studied.

Fig. 10 shows the difference between thermal contact resistance with and without consideration of thermal radiation through gaps, and the deviation δ is defined as Eq. (7):

$$\delta = \frac{R_{nonra} - R_{ra}}{R_{nonra}} \tag{7}$$

where R_{nonra} and R_{ra} represent thermal contact resistance without and with consideration of thermal radiation, respectively. The interface average temperature equals to $(T_I + T_{II})/2$.

We can find that all deviations are positive in Fig. 10, which is reasonable and reveals that thermal radiation can enhance the heat transfer between interfaces, thereby, predicted thermal contact resistance with thermal radiation is lower than that without thermal radiation between the contact interfaces. In addition, with the increase in loading pressure, the actual contact surface increases, thus, the gaps reduces through which radiant heat transfer between bottom and top
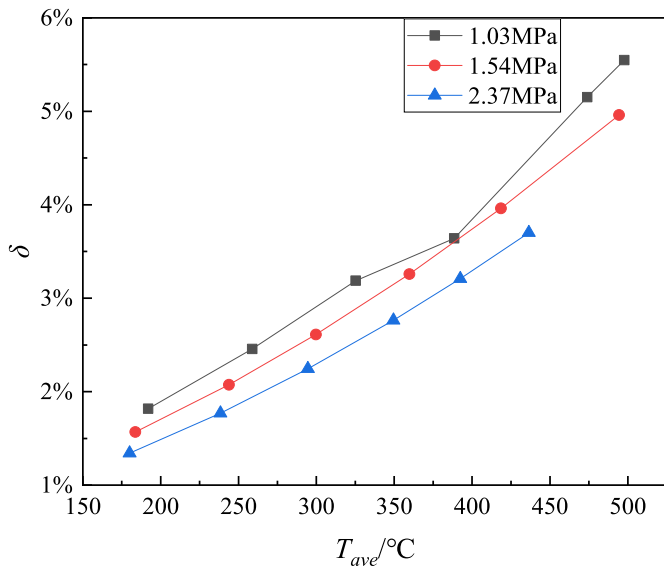
Fig. 10. Difference between TCR with and without thermal radiation.

Fig. 11. Percentage of solid heat conduction.

surfaces occurs. So the effect of thermal radiation decreases. Generally speaking for the cases studied, the radiative heat transfer occupies about 1% of the total heat transfer between the top and bottom bodies, with the maximum of 1.2% at pressure of 1.03 MPa and the minimum of 0.7% at pressure of 2.37 MPa.

On the other hand, the differences in Fig. 10 increase with an increase in interface average temperature and decreases with an increase in loading pressure. The reason is that when temperature increases, the effect of thermal radiation increases. When interface average temperature is beyond 400 °C, the deviation caused by thermal radiation exceeds 3% even though the loading pressure reaches to 2.37 MPa, whereas in a low loading pressure 1.03 MPa, the deviation exceeds 3% at an interface average temperature of 325 °C, which reveals that an increasing loading pressure can weaken the effect of thermal radiation on thermal contact resistance. As Madhusudana pointed out in Ref. [1] that thermal radiation may usually be neglected unless the temperatures at the joint are in excess of 300 °C, unless the temperature drop across the interface is large.

4.5. Percentage of solid heat conduction

Heat conduction between two contact interfaces can be divided into solid heat conduction, thermal radiation and air heat conduction when the convection is neglected [1]. To the author's knowledge, it lacks information of how much percentage of each one is at different conditions. Fig. 11 shows the percentage of solid heat conduction for the seven cases. The percentage is the ratio of the heat transfer rate through solid contact spots in contact interfaces divided by the overall heat transfer rate through the contact interfaces.

We can find from Fig. 11 that the percentage of heat transfer rate through solid contact spots increases with an increase in loading pressure, but decreases with an increase in interface average temperature. It is because a larger loading pressure contributes to more actual contact spots, thereby more heat transfer rate flows through the solid contact spots. On the other hand, when the interface average temperature increases, thermal conductivity of air increases, so the heat transfer rate through the air gaps increases, which inspires us that if we want to reduce TCR between the contact interfaces, the gaps should be filled by materials with a relatively high thermal conductivity. It should be mentioned that for the cases studied the solid thermal conductivity is about 10 W·m^{-1}·K^{-1} (see Table 3), and the solid heat conduction only occupies a small part, smaller than 17% even the loading pressure increases to 2.37 MPa.
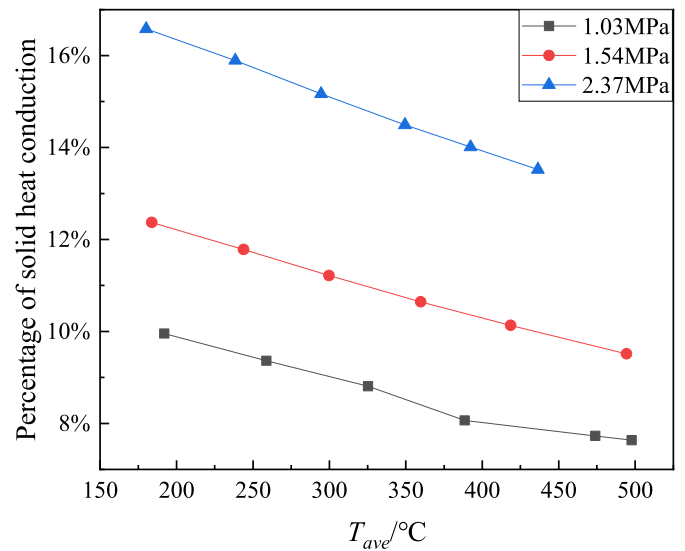
4.6. Thermal contact resistance calculation expression

Fig. 12 summarizes the dependency of thermal contact resistance with the interface average temperature and loading pressure. As explained above, thermal contact resistance of the composite pair declines with the increasing temperature and loading pressure. For this composite pair under the given computational cases in this paper, thermal contact resistance is in a range of 9.8×10^{-4} - 5.7×10^{-4} K·m^2·W^{-1}.

By using least square method, following curve-fitted expression is obtained

$$h = c_1 \left(\frac{T_{ave}}{T} \right)^{c_2} \left(\frac{P}{E} \right)^{c_3} \tag{8}$$

where h is thermal contact conductance and is the reciprocal of TCR. T_{ave} is the interface average temperature. P is loading pressure, MPa and E is elastic modulus at T (=298K), 60 GPa. The fitting parameters, c_1, c_2, c_3, are listed at Table 5.
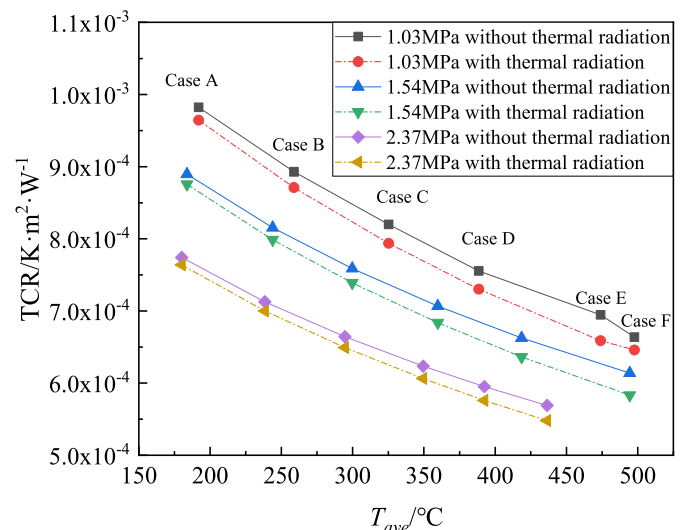
Fig. 12. Thermal contact resistance at different Cases.

Table 5
Fitting parameters.

	$c_1/\text{W}\cdot\text{K}^{-1}\cdot\text{m}^{-2}$	c_2	c_3
Without thermal radiation	17770.1	0.73	0.29
With thermal radiation	14281.9	0.79	0.27

4.7. Validation for numerical model

Finally some validation of the numerical model is presented. The validation experiments are performed by a three-element system. This system consists of three parts: surface topography measurement facility (microscope named Bruker Contour GT-K with a vertical resolution of 0.1 nm specified by the manufacturer), thermal conductivity measurement facility (Hot Disk, TPS2500S) and a home-made test-piece temperature distribution measurement facility, which is shown in Fig. 13. This apparatus is based on 1D steady-state heat flux method to measure the temperature profiles of two contact specimens, and the temperatures of contact interfaces are obtained by extrapolating the measured temperatures. Each specimen is 20 mm in height and 24 mm in radius. Each specimen has four temperature measurement holes. The holes are uniformly distributed around the circle of the middle height. The holes to mount thermocouples are 1 mm in radius and 12 mm in depth. The following equations are used to calculate experimental thermal contact resistance:

$$T_{Iexp} = T_{down} - \frac{q}{\lambda_{down}}\Delta x_1 \tag{9}$$

$$T_{IIexp} = T_{up} + \frac{q}{\lambda_{up}}\Delta x_2 \tag{10}$$

$$R_{exp} = \frac{T_I - T_{II}}{q} \tag{11}$$

where, Δx_1 and Δx_2 are the distances from the measurement spots to the contact interface.

Table 6 shows comparisons between numerical results and experimental results under 1.54 MPa. It can be found that the numerical results of interface temperatures agree well with the experimental results. The deviations between experimental and numerical TCR are around 10%, which is totally acceptable for engineering applications.

The reliability of our numerical results can be further illustrated from following three aspects. First, different from many other numerical models where the surface topography of the studied materials is often assumed or by some theoretical model, in the present study the surface topography of the studied materials is measured by a high precision instrument, the optical microscope named Bruker Contour GT-K with vertical resolution 0.1 nm. This action can guarantee that the input surface roughness data to reconstruct numerical rough surfaces are reliable. Second, the software Abaqus and several practical treatments (for example the single contact technique) have been used in Ref. [27] by our group to predict the thermal contact resistances of Ti–6Al–4V alloy, for which the experimental measurements have also been conducted. The deviation between test data and numerical prediction are all below 10%. Third, from our predicted results at least we can show qualitative agreement of our numerical results with previous results in two points. The first point is the actual contact surface percentage for two nominally contact surfaces. Madhusudana and Ling [1] and Bowden and Tabor [45] all pointed out that the actual contact area of most metallic surfaces is only about 1–2% of the nominal contact area even at relatively high contact pressures of the order of 10 MPa. Our numerical prediction agrees with this conclusion quite well. The second point is the thermal contact resistance variation trend with surface temperature. It can be seen from Fig. 9, under the loading pressure of 1.54 MPa, our predicted thermal contact resistance decreases from 8.9×10^{-4} K m^2 W^{-1} to 6.1×10^{-4} K m^2 W^{-1} (reduction by about 31%) when the interface temperature increases from 184 °C to 494 °C. Liu et al. [34] conducted an experimental study on thermal contact resistance between C/C composite and Inconel 600. In their experiments, under the contact pressure of 1.41 MPa, the interface TCR decreased from 1.76×10^{-4} K m^2 W^{-1} to 1.19×10^{-4} K m^2 W^{-1} (reduction by 32%) when the interface temperature increased from 176 °C to 580 °C. In roughly the same variation range of temperature and at roughly the same pressure, for roughly the same type of materials the reduction percentages are roughly the same. In sum up, for the 8-harness satin woven composite with surface averaged roughness around our tested value, the above TCR values should be applicable. Of course to meet the requirement of wide engineering application, our tested range of parameters is quite limited, and it can be extended toward two directions. First the environmental pressure may be extended to vacuum situation to meet the requirement of space flight. Second the surface averaged roughness range should be
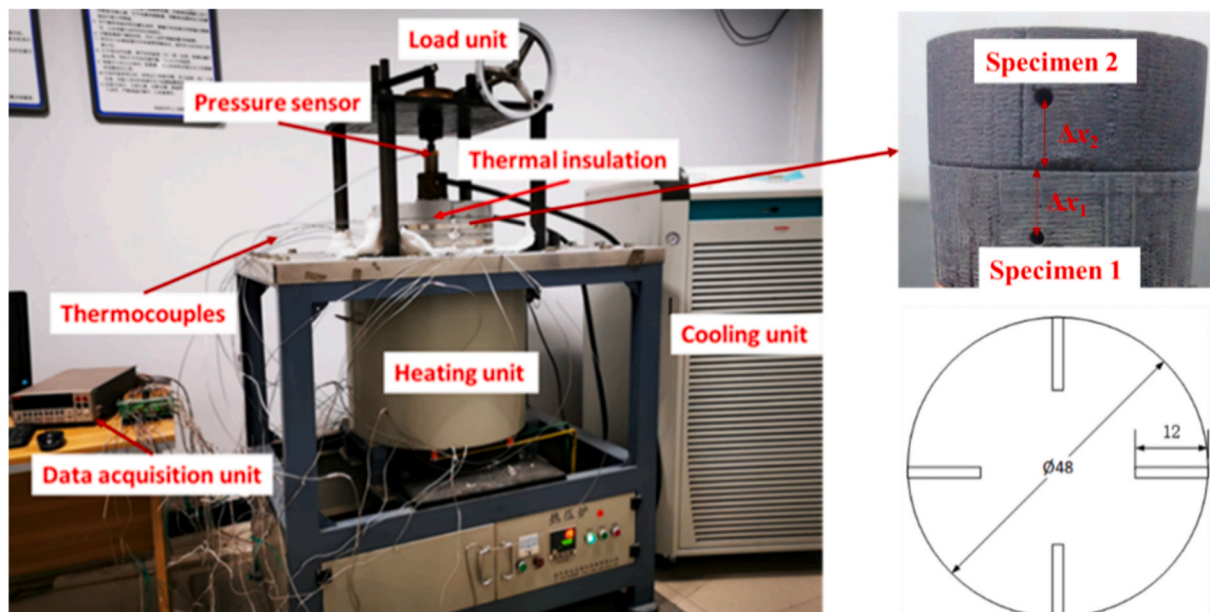
Fig. 13. Experimental apparatus for specimen temperature measurement.

Table 6
Numerical and experimental results under 1.54 MPa.

	T_{I}/°C			T_{II}/°C			q	TCR $\times 10^4$ (K·m^2·W^{-1})		
	Num.	Exp.	δ_1	Num.	Exp.	δ_2	W·m^{-2}	Num.	Exp.	δ_3
Case A	189.8	189.2	0.34%	177.6	178.2	−0.30%	13681.3	8.89	8.03	10.71%
Case B	252.1	251.3	0.29%	235.6	236.7	−0.48%	20227.5	8.16	7.22	12.90%
Case C	309.9	309.0	0.29%	289.5	290.9	−0.45%	26780.9	7.59	6.76	12.18%
Case D	371.6	370.6	0.27%	347.8	349.4	−0.44%	33649.7	7.07	6.32	11.87%
Case E	432.1	431.3	0.18%	405.0	406.7	−0.42%	40958.9	6.62	6.02	10.04%
Case F	509.5	509.0	0.11%	479.3	480.9	−0.34%	49326.1	6.14	5.70	7.69%

wider to cover all possible cases that satin woven pierced composite may have.

5. Conclusions

This paper conducts the simulation of thermal contact resistance of a pair of 8-harness satin woven pierced composite when the gap medium is air. The simulation is based on the measured surface topography. The main findings can be listed as follows:

(1) Thermal contact resistance of the composite decreases with an increase in both temperature and loading pressure. For the cases studied, increase loading pressure from 1.03 MPa to 2.37 MPa will lead to increase TCR about 21%; while increase temperature from 200 °C to 500 °C will lead to a decrease of TCR by about 33%.

(2) The predicted thermal contact resistance with thermal radiation is lower than that without thermal radiation when the gaps between contact interfaces are filled with air. With an increase in interface temperature, the effect of thermal radiation on the predicted thermal contact resistance will increase, especially for low loading pressure conditions.

(3) For the cases studied with solid thermal conductivity around 10 W·m^{-1}·K^{-1}, the portion of solid heat conduction only takes a small part (smaller than 17% under all computational cases in this paper). This percentage undergoes a decrease with increase in temperature while an increase with an increase in loading pressure.

(4) For this composite pair studied, the averaged surface roughness of the two contact interfaces is 12.30 μm and 10.54 μm, respectively. The predicted thermal contact resistances within interface temperature range from about 180 to 500 °C and loading pressure range from 1.03 to 2.37 MPa vary in the range of 9.8×10^{-4} - 5.7×10^{-4} K·m^2·W^{-1}.

Declaration of competing interest

The authors declare that they have no known competing financial interests or personal relationships that could have appeared to influence the work reported in this paper.

Appendix. A: Mechanics governing equation

(A.1) Elastic stress-strain equation

For an elastic body, the governing equations are shown in Eqs.(A.1)-(A.3),

$$\frac{\partial \sigma_x}{\partial x} + \frac{\partial \tau_{yx}}{\partial y} + \frac{\partial \tau_{zx}}{\partial z} + \overline{f_x} = 0 \tag{A.1}$$

$$\frac{\partial \tau_{xy}}{\partial x} + \frac{\partial \sigma_y}{\partial y} + \frac{\partial \tau_{zy}}{\partial z} + \overline{f_y} = 0 \tag{A.2}$$

$$\frac{\partial \tau_{xz}}{\partial x} + \frac{\partial \tau_{yz}}{\partial y} + \frac{\partial \sigma_z}{\partial z} + \overline{f_z} = 0 \tag{A.3}$$

where, $\overline{f_x}, \overline{f_y}, \overline{f_z}$ are components of unit body force in x, y, z direction. τ_{ij} is the shear stress, and $\sigma_i (i = x, y, z)$ is normal stress. The stress-strain relation follows the Hooke's law as shown in Eq A.4,

$$d\sigma_{ij} = D^e_{ijkl} d\varepsilon^e_{kl} \tag{A.4}$$

In the equation, ε^e_{kl} is the elastic strain. D^e_{ijkl} is the elasticity matrix. In isotropic case, Eq.(A.4) can be expanded into Eq.(A.5),

$$
\begin{bmatrix} \sigma_x \\ \sigma_y \\ \sigma_z \\ \tau_{xy} \\ \tau_{xz} \\ \tau_{yz} \end{bmatrix} = \frac{E}{1+\nu} \begin{bmatrix} \frac{1-\nu}{1-2\nu} & \frac{\nu}{1-2\nu} & \frac{\nu}{1-2\nu} & 0 & 0 & 0 \\ \frac{\nu}{1-2\nu} & \frac{1-\nu}{1-2\nu} & \frac{\nu}{1-2\nu} & 0 & 0 & 0 \\ \frac{\nu}{1-2\nu} & \frac{\nu}{1-2\nu} & \frac{1-\nu}{1-2\nu} & 0 & 0 & 0 \\ 0 & 0 & 0 & \frac{1}{2} & 0 & 0 \\ 0 & 0 & 0 & 0 & \frac{1}{2} & 0 \\ 0 & 0 & 0 & 0 & 0 & \frac{1}{2} \end{bmatrix} \begin{bmatrix} \varepsilon_x \\ \varepsilon_y \\ \varepsilon_z \\ \gamma_{xy} \\ \gamma_{xz} \\ \gamma_{yz} \end{bmatrix}
\tag{A.5}
$$

where E and ν are the Young's modulus and the Poisson's ratio, respectively. γ_{ij} is the shear strain. These parameters can be given as functions of temperature and of other predefined fields, if necessary. In this paper, these parameters are treated as independent with temperature.

(A.2) Plastic stress-strain equation

In this paper, the classical metal plasticity model is applied to solve plastic deformation. This model in Abaqus is the "incremental" theory in which the mechanical strain is decomposed into an elastic part and a plastic (inelastic) part, and the mathematical expression is shown by Eq.(A.6),

$$
d\varepsilon_{ij} = d\varepsilon_{ij}^p + d\varepsilon_{ij}^e
\tag{A.6}
$$

where ε_{ij} is the total mechanical strain, ε_{ij}^p is the strain related to the plastic deformation and ε_{ij}^e is the elastic strain. Besides, the above equation always follows the generalized Hooke's law. So the incremental stress-strain relation can be described with Eq.(A.7) and Eq.(A.8),

$$
d\sigma_{ij} = D_{ijkl}^{ep} d\varepsilon_{kl}
\tag{A.7}
$$

$$
D_{ijkl}^{ep} = D_{ijkl}^e - D_{ijkl}^p
\tag{A.8}
$$

where D_{ijkl}^p is the plasticity matrix, it can be expressed by Eq.(A.9) with matrix form under Cartesian coordinates.

$$
\mathbf{D}_p = \frac{9G^2 \mathbf{S}\mathbf{S}^\mathrm{T}}{\sigma_s^2 (3G + E_p)}
\tag{A.9}
$$

where E_p is the plasticity modulus, $E_p = \frac{EE_t}{E-E_t}$, $E_t = \frac{d\sigma}{d\varepsilon}$. E_t is the slope of the stress-strain curve in the plastic region and will in general change during a deformation. σ_s is elastoplasticity stress. The shear modulus, G, can be expressed in terms of E and ν as $G = \frac{E}{2(1+\nu)}$. For deflection stress tensor $\mathbf{S}$ and its components, they have following expressions in Eq.(A.10) and Eq.(A.11),

$$
\mathbf{S} = \begin{bmatrix} s_x & s_y & s_z & \tau_{xy} & \tau_{yz} & \tau_{zx} \end{bmatrix}^\mathrm{T}
\tag{A.10}
$$

$$
s_i = \sigma_i - \frac{1}{3}(\sigma_x + \sigma_y + \sigma_z) \quad (i = x, y, z)
\tag{A.11}
$$

References

[1] C.V. Madhusudana, F.F. Ling, Thermal Contact Conductance, second ed., Springer, New York, 2013.

[2] L. Pan, D.B. Bogy, Data storage: heat-assisted magnetic recording, Nat. Photon. 3 (4) (2009) 189–190.

[3] M. Grujicic, C.L. Zhao, E.C. Dusel, The effect of thermal contact resistance on heat management in the electronic packaging, Appl. Surf. Sci. 246 (1–3) (2005) 290–302.

[4] G. Caruso, F. Giannetti, A. Naviglio, An experimental study on the air-side heat transfer coefficient and the thermal contact conductance in finned tubes, Heat Tran. Eng. 36 (2) (2014) 212–221.

[5] C. Madhusudana, W.W. Cheng, Decrease in thermal contact conductance and the contact pressure of finned-tube heat exchangers assembled with different size bullets, J. Heat Transf. Trans. Asme 129 (7) (2007) 907–911.

[6] M. Dillig, T. Biedermann, J. Karl, Thermal contact resistance in solid oxide fuel cell stacks, J. Power Sources 300 (2015) 69–76.

[7] M. Khandelwal, M.M. Mench, Direct measurement of through-plane thermal conductivity and contact resistance in fuel cell materials, J. Power Sources 161 (2) (2006) 1106–1115.

[8] D. Gilmor, Spacecraft thermal control handbook. Vol. vol. 1. Fundamental Technologies. 2002: El Segundo, California, Aerospace Press.

[9] T. Huang, Q.W. Wu, J.S. Liang, et al., Calculation of thermal contact resistance for space camera, Chin. J. Optics Appl. Optics 2 (4) (2009) 334–339.

[10] H.S. Ge, J. Liu, Keeping smartphones cool with gallium phase change material, J. Heat Trans. Trans. Asme 135 (5) (2013).

[11] S.M.S. Wahid, C.V. Madhusudana, Thermal contact conductance: effect of overloading and load cycling, Int. J. Heat Mass Tran. 46 (21) (2003) 4139–4143.

[12] Y.Z. Li, C.V. Madhusudana, E. Leonardi, Experimental investigation of thermal contact conductance: variations of surface microhardness and roughness, Int. J. Thermophys. 19 (6) (1998) 1691–1704.

[13] E.E. Marotta, L.S. Fletcher, Thermal contact conductance of refractory ceramic coatings, J. Thermophys. Heat Tran. 10 (1) (1996) 10–18.

[14] M.A. Lambert, L.S. Fletcher, Metallic coatings for enhancement of thermal contact conductance, J. Thermophys. Heat Tran. 8 (2) (1994) 341–348.

[15] P. Zhang, T. Cui, Q. Li, Effect of surface roughness on thermal contact resistance of aluminium alloy, Appl. Therm. Eng. 121 (2017) 992–998.

[16] R.F. Dou, T.R. Ge, X.L. Liu, et al., Effects of contact pressure, interface temperature, and surface roughness on thermal contact conductance between stainless steel surfaces under atmosphere condition, Int. J. Heat Mass Tran. 94 (2016) 156–163.

[17] R. Joseph, J. Peter, S.S. Kumar, et al., Effect of thermal and load cycle on thermal contact conductance across dissimilar joints at cryogenic temperature, Appl. Therm. Eng. 111 (2017) 1622–1628.

[18] P. Zhang, Y. Xuan, Q. Li, A high-precision instrumentation of measuring thermal contact resistance using reversible heat flux, Exp. Therm. Fluid Sci. 54 (2014) 204–211.

[19] P. Sadowski, S. Stupkiewicz, A model of thermal contact conductance at high real contact area fractions, Wear 268 (1–2) (2010) 77–85.

[20] M.A. Lambert, L.S. Fletcher, Thermal contact conductance of non-flat, rough, metallic coated metals, Journal of Heat Transfer-Transactions of the Asme 124 (3) (2002) 405–412.

[21] M. Ahmadi, M. Fakoor Pakdaman, M. Bahrami, Analytical investigation of thermal contact resistance (TCR) behavior under time-dependent thermal load, in: 32nd Thermal Measurement, Modeling & Management Symposium (SEMI-THERM), IEEE, 2016, pp. 15–21, 15-21.

[22] C.V. Madhusudana, Accuracy in thermal contact conductance experiments - the effect of heat losses to the surroundings, Int. Commun. Heat Mass Tran. 27 (6) (2000) 877–891.

[23] V. Gopal, M.J. Whiting, J.W. Chew, et al., Thermal contact conductance and its dependence on load cycling, Int. J. Heat Mass Tran. 66 (2013) 444–450.

[24] B. Dongmei, C. Huanxin, L. Shanjian, et al., Measurement of thermal diffusivity/ thermal contact resistance using laser photothermal method at cryogenic temperatures, Appl. Therm. Eng. 111 (2017) 768–775.

[25] X. Zhang, P.Z. Cong, M. Fujii, A study on thermal contact resistance at the interface of two solids, Int. J. Thermophys. 27 (3) (2006) 880–895.

[26] J.J. Gou, X.J. Ren, Y.J. Dai, et al., Study of thermal contact resistance of rough surfaces based on the practical topography, Comput. Fluids 164 (2018) 2–11.

[27] Y.J. Dai, J.J. Gou, X.J. Ren, et al., A test-validated prediction model of thermal contact resistance for Ti-6Al-4V alloy, Appl. Energy 228 (2018) 1601–1617.

[28] X.J. Ren, Y.J. Dai, J.J. Gou, et al., Numerical prediction of thermal contact resistance of 3D C/C-SiC needled composites based on measured practical topography, Int. J. Heat Mass Tran. 131 (2019) 176–188.

[29] J.J. Gou, X.J. Ren, W.Z. Fang, et al., Two small unit cell models for prediction of thermal properties of 8-harness satin woven pierced composites, Compos. B Eng. 135 (2018) 218–231.

[30] K. Wei, X. Cheng, F. Mo, et al., Design and analysis of integrated thermal protection system based on lightweight C/SiC pyramidal lattice core sandwich panel, Mater. Des. 111 (2016) 435–444.

[31] Y. Ma, B. Xu, M. Chen, et al., Optimization design of built-up thermal protection system based on validation of corrugated core homogenization, Appl. Therm. Eng. 115 (2017) 491–500.

[32] D. Glass, Ceramic matrix composite (CMC) thermal protection systems (TPS) and hot structures for hypersonic vehicles, in: 15th AIAA International Space Planes and Hypersonic Systems and Technologies Conference, 2008.

[33] M. Marchetti, P. Testa, F.R. Torrisi, Measurement of thermal-conductivity and thermal contact resistance in composite-materials for space applications, ESA J. Eur. Space Agency 12 (3) (1988) 369–377.

[34] D. Liu, Y. Luo, X. Shang, Experimental investigation of high temperature thermal contact resistance between high thermal conductivity C/C material and Inconel 600, Int. J. Heat Mass Tran. 80 (2015) 407–410.

[35] W.Z. Fang, Studies on lattice Boltzmann simulations for transport phenomena in porous media, multiphase flow and phase change problems, in: School of Energy & Power Engineering, Xi'an Jiaotong University, Dec, 2018.

[36] J.B. Xu, K. Läuger, R. Möller, et al., Heat transfer between two metallic surfaces at small distances, J. Appl. Phys. 76 (11) (1994) 7209–7216.

[37] V.A. Yastrebov, G. Anciaux, J.F. Molinari, et al., From infinitesimal to full contact between rough surfaces: evolution of the contact area, Int. J. Solid Struct. 52 (2015) 83–102.

[38] G. Carbone, F. Bottiglione, Asperity contact theories: do they predict linearity between contact area and load? J. Mech. Phys. Solid. 56 (8) (2008) 2555–2572.

[39] V.A. Yastrebov, G. Anciaux, J.-F.J.T.I. Molinari, On the accurate computation of the true contact-area in mechanical contact of random rough surfaces, Tribol. Int. 114 (2017) 161–171.

[40] J.A. Greenwood, J.B.P. Williamson, Contact of nominally flat surfaces, Proc. Math. Phys. Eng. Sci. 295 (1442) (1966) 300–319.

[41] A. Bush, R. Gibson, T. Thomas, The elastic contact of a rough surface, Wear 35 (1) (1975) 87–111.

[42] J.I. McCool, Comparison of models for the contact of rough surfaces, Wear 107 (1) (1986) 37–60.

[43] B.N.J. Persson, Elastoplastic contact between randomly rough surfaces, Phys. Rev. Lett. 87 (11) (2001).

[44] J. Greenwood, A simplified elliptic model of rough surface contact, Wear 261 (2) (2006) 191–200.

[45] F.P. Bowden, D. Tabor, The Friction and Lubrication of Solids, vol. 1, Oxford university press, 2001.